Ambipolar charge transport in quasi-free-standing monolayer graphene on SiC obtained by gold intercalation

Ambipolar charge transport in quasi-free-standing monolayer graphene on SiC obtained by gold intercalation

Kyung Ho Kim,[1,*] Hans He,[1] Claudia Struzzi,[2] Alexei Zakharov,[2] Cristina E. Giusca,[3] Alexander Tzalenchuk,[3,4] Yung Woo Park,[5,6] Rositsa Yakimova,[7] Sergey Kubatkin,[1] and Samuel Lara-Avila[1,3,†]

[1]*Department of Microtechnology and Nanoscience, Chalmers University of Technology, SE-412 96, Gothenburg, Sweden*
[2]*MAX IV Laboratory, 221 00, Lund, Sweden*
[3]*National Physical Laboratory, Hampton Road, Teddington TW11 0LW, United Kingdom*
[4]*Royal Holloway, University of London, Egham TW20 0EX, United Kingdom*
[5]*Institute of Applied Physics, Seoul National University, Seoul 08826, Korea*
[6]*Department of Physics and Astronomy, University of Pennsylvania, Philadelphia, Pennsylvania 19104, USA*
[7]*Department of Physics, Chemistry and Biology, Linköping University, 581 83 Linköping, Sweden*

(Received 2 June 2020; revised 4 August 2020; accepted 8 September 2020; published 5 October 2020)

We present a study of quasi-free-standing monolayer graphene obtained by intercalation of Au atoms at the interface between the carbon buffer layer (Bu-L) and the silicon-terminated face (0001) of 4*H*-silicon carbide. Au intercalation is achieved by deposition of an atomically thin Au layer on the Bu-L followed by annealing at 850 °C in an argon atmosphere. We explore the intercalation of Au and decoupling of the Bu-L into quasi-free-standing monolayer graphene by surface science characterization and electron transport in top-gated electronic devices. By gate-dependent magnetotransport we find that the Au-intercalated buffer layer displays all properties of monolayer graphene, namely gate-tunable ambipolar transport across the Dirac point, but we find no observable enhancement of spin-orbit effects in the graphene layer, despite its proximity to the intercalated Au layer.

DOI: 10.1103/PhysRevB.102.165403

I. INTRODUCTION

Epitaxial graphene grown on SiC (epigraphene) is a promising route for scalable graphene electronics. The silicon-terminated face (0001) offers the possibility to grow continuous, single-crystal graphene over wafer scale, as demonstrated for hexagonal SiC polytypes 4*H* and 6*H* [1,2]. A challenge for epigraphene electronics is that the monolayer on the silicon face is heavily *n*-type doped, with a typical intrinsic doping $n \sim 1 \times 10^{13}$ electrons/cm^2 pinned by the SiC substrate [3], and this complicates tuning the carrier density of epigraphene with, e.g., electrostatic gates [3–5]. The high doping originates from the structure of the interface between SiC and the epigraphene, where an interface layer, the so-called carbon buffer layer (Bu-L), serves as a source of donorlike states that result in *n*-type doping [6].

A route aiming at controlling the graphene-SiC interaction is by intercalation of hydrogen at the epigraphene-SiC interface [7,8]. In this intercalation process, epigraphene is subjected to a thermal annealing step in a hydrogen-containing atmosphere. At high temperatures, hydrogen atoms migrate into the interface between the Bu-L and SiC, breaking the Si–C bonds and saturating the Si dangling bonds resulting in the lifting of the graphene/Bu-L into quasi-free-standing (QFS) bilayer graphene [7,8]. The same process can be applied to the Bu-L which, remarkably, recovers all attributes of monolayer graphene (MLG) after hydrogen intercalation [7–12]. Yet, the resulting QFS monolayer might still suffer from strong interaction with SiC, due to spontaneous polarization of the hexagonal substrate, leading to heavy *p*-type doping [6]. Besides hydrogen, other atomic species can be intercalated [13]. Among all intercalants, Au has shown the possibility to result in *n*-type or *p*-type doped graphene depending on the amount of gold that is intercalated [14,15]. In addition to controlling the doping type, Au is attractive because it could lead to enhancing spin-orbit interaction (SOI) in graphene, which holds promises for a variety of spin-related phenomena in graphene [16–19]. From a practical point of view, the chemical inertness of Au is also attractive, because it can enable the *ex situ* processing of intercalated graphene into devices.

We report electron transport studies complemented by surface science analysis of QFS graphene obtained by Au intercalation at the Bu-L/SiC interface [Fig. 1(a)]. We use the epitaxial Bu-L grown on 4*H*-SiC (0001) substrates and decouple it from the SiC substrate by deposition of Au atoms on the surface followed by a thermal drive-in at $T = 850\,^{\circ}$C. The strong interaction between Au and the Bu-L allows for smooth deposition of Au monolayers, without Au agglomeration into clusters [20]. After Au intercalation, we

*kyungh@chalmers.se
†samuel.lara@chalmers.se

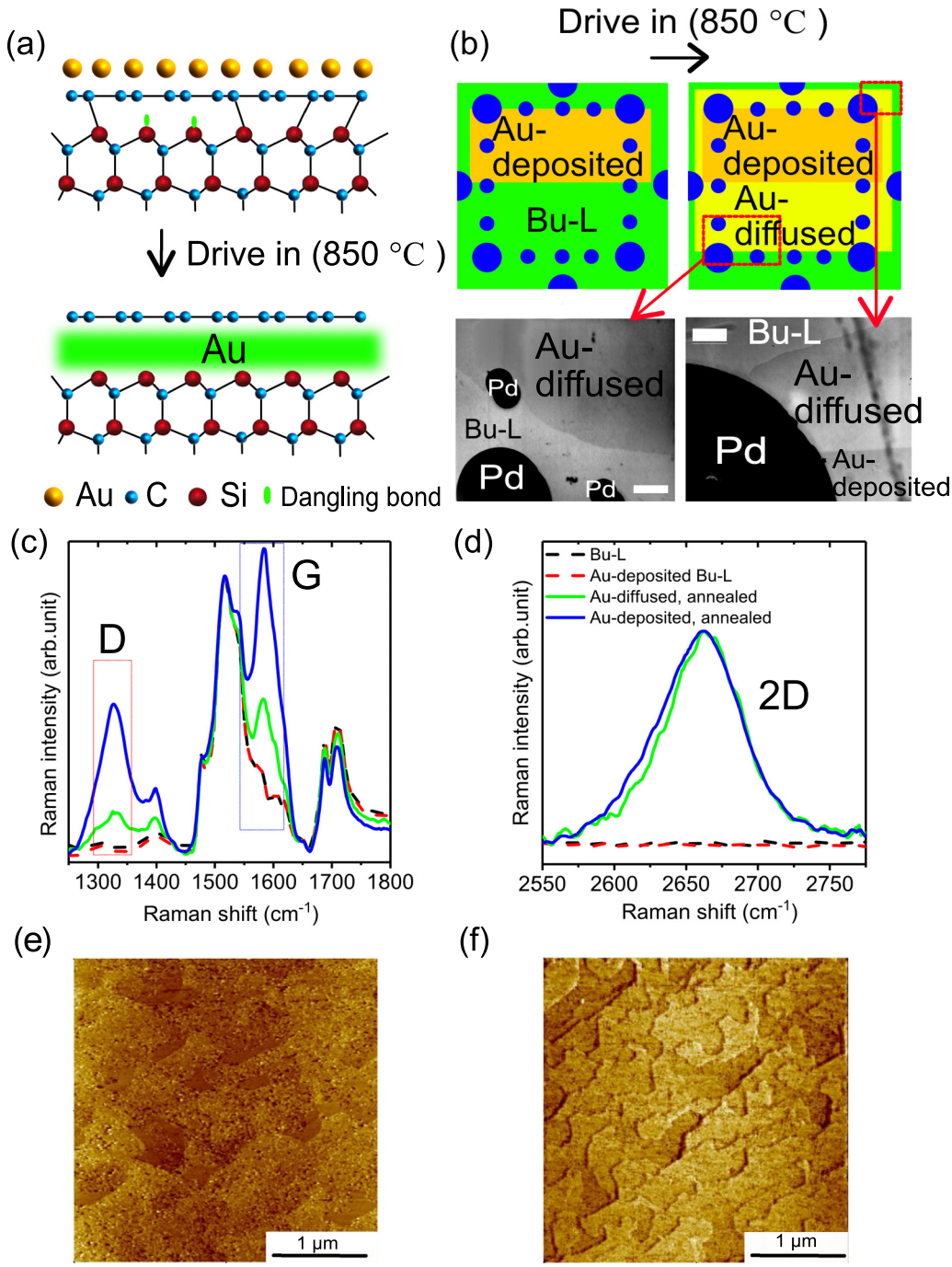

FIG. 1. Au-intercalated quasi-free-standing monolayer graphene. (a) A schematic of Au atoms on top of the Bu-L and intercalation of Au atoms after thermal drive, lifting the Bu-L from SiC (0001) to produce QFS monolayer graphene. (b) Schematics of Au atoms (yellow) on half of the Bu-L substrate before thermal drive, and diffusion of Au (light yellow, Au diffused) after thermal drive. The blue circles are Pd contacts. The bottom figures are optical micrographs of the areas in the red boxes, showing the diffusion of Au over millimeter lengths. The black circles are Pd contacts and the scale bar is 100 μm. (c), (d) Raman spectroscopy around the Raman *D* and *G* peaks (c) and 2D peaks. The spectra given for the Bu-L (black), Au-deposited Bu-L (red), Au-diffused area (green), and Au-deposited area after intercalation (blue) show the emergence of graphene *D*, *G*, and 2D peaks after decoupling the Bu-L. (e), (f) STM topography images (z range = 13 nm) after 4-Å Au intercalation, where the Au-deposited area shows Au clusters (e) and the Au-diffused area (f) is cluster free with clear terraces on the surface.

study electronic transport properties of top-gated devices and find that Au-intercalated Bu-L displays properties of monolayer graphene, with a zero-gate doping level located at $n = 0.7$–$1.2 \times 10^{12}\,\mathrm{cm}^{-2}$.

II. RESULTS AND DISCUSSION

A. Intercalation of gold

To prepare Au-intercalated QFS graphene, we start with 7 mm × 7 mm SiC/Bu-L substrates onto which we deposit Au

on about half of the chip area (5 mm × 2.5 mm) [Fig. 1(b)]. We have studied deposition of two different Au thickness, $t_{Au} = 4$ Å and 8 Å, in two SiC/Bu-L substrates. Our deposition conditions result in a cluster-free Au layer on the surface, as evidenced by atomic force microscopy (AFM) (Fig. S1) [20,21], with an rms roughness of 1 Å. Despite the homogeneous coverage of Au on the Bu-L surface, such layers are electrically not conductive. After Au deposition, the intercalation step at $T = 850\,^{\circ}$C turns the surface electrically conductive, showing resistance values on the order of few kOhms (∼3–20 kΩ). This onset of electrical conductivity occurs not only on the Au deposited area, but on the rest of the surface as well (i.e., where Au was originally not present), pointing to diffusion of Au across the surface. Together with the change in electrical conductance, optical inspection [22] of the chip allows one to see that the thermal intercalation step leads to lower transparency of the surface, even millimeters away from the Au-deposited area [Fig 1(b)]. Raman spectroscopy ($\lambda = 638$ nm) readily showed the emergence of the graphene 2D peak (2662 cm^{-1}) everywhere on surface, with full width at half maximum (FWHM) = 68 cm^{-1} on the Au-deposited area and FWHM = 63 cm^{-1} on areas located few millimeters away [Figs. 1(c) and 1(d)] [14]. Both the Raman spectra and the onset of electrical conductivity of the surface after the annealing step serve as a strong indication that the Bu-L has decoupled from the substrate and transformed into monolayer graphene everywhere on the surface. Scanning tunneling microscopy (STM) analysis shows that the Au-deposited area displays a granular morphology consistent with the presence of Au clusters on the surface [Fig. 1(e)], which gradually disappear as one moves away from that area. Far from the deposited area, the surface appears free of Au clusters, with a terraced surface typical of SiC/Bu-L [Fig. 1(f)], yet being electrically conductive. As we describe below, this area corresponds to regions where Au has diffused and intercalated at the buffer-SiC interface, and we name this the Au-diffused region [Fig. 1(b)].

Studies at synchrotron facilities confirm the intercalation of gold atoms in both the Au-deposited and Au-diffused area. Figure 2(a) is the low-energy electron microscopy (LEEM) image at the boundary of the Au-deposited and Au-diffused areas after thermal drive-in of 4 Å Au. The contrast in the two regions is due to the slightly different amount of intercalated gold (the darker gray color scale corresponds to lower gold content). In agreement with Raman spectroscopy and electrical transport, these measurements show that decoupling of the Bu-L occurs on both the gold-deposited and gold-diffused areas, as seen through the quenching of the $6\sqrt{3} \times 6\sqrt{3}R30^{\circ}$ pattern in low-energy electron diffraction (LEED) [Figs. 2(b) and 2(c)]; (see Fig. S5 for the LEED of the buffer layer) [21]. The diffractograms also show the hexagonal honeycomb structure of graphene after the thermal drive-in for both Au-deposited and Au-diffused areas. In contrast to the micro LEED presented by Forti *et al.* [15], we do not observe a (20 × 20) ordering of Au atoms over (19 × 19) SiC unit cells. This may evidence the lack of long-range order of Au atoms. The LEEM intensity IV curves from both sides of the boundary are shown in Fig. 2(d); the dip at 5.5 eV results from the intercalation and consequent formation of QFS graphene [23]. The presence of Au is confirmed by micro x-ray photoelectron microspectroscopy results (micro-XPS), showing the gradual weakening of the Au signal far from the boundary [Fig. 2(e)]. Moreover, the $C1s$ micro-XPS spectra (Fig. 2(f)) shows that charge transfer from gold to graphene increases the separation between carbon peaks from graphene and the SiC substrate [13].

B. Ambipolar charge transport

To assess the electrical properties of the Au-intercalated QFS graphene we have fabricated microsized devices on the two substrates ($t_{Au} = 4$ Å, 8 Å). In total, we have studied eight devices (labeled as D1–D8), placed on the Au-deposited and Au-diffused areas of the substrates. Devices were made by conventional electron-beam lithography (EBL) and oxygen plasma etching. For gated devices, we have used dry-transferred hexagonal boron nitride (*h*-BN) (thickness ∼20 nm) followed by atomic layer deposition of Al_2O_3 (38 nm) as a dielectric, and Ti/Au as a gate electrode. Figures 3(a)–3(c) depict the schematic structure of the top-gated devices in the top and edge contact configurations together with an optical micrograph of D1. To avoid further processing steps, *h*-BN was not patterned, and the geometry of the devices is dictated by the shape of the transferred *h*-BN flakes. Magnetotransport properties of the devices were measured by the van der Pauw method in a gas-flow cryostat down to $T = 2$ K. We quantified the Hall carrier density and mobility as $n_H = 1/eR_H$ and $\mu_H = R_H/\rho_{XX}(B = 0)$, using $R_H = dR_{XY}/dB|_{B=0}$, respectively.

We found that devices made on the Au-deposited area are insensitive to the gate voltage, due to screening of the electric field by the Au layer present directly atop the graphene layer. Gate response is only observed in those devices fabricated on the Au-diffused area, where Au is absent on top of the graphene layer according to STM scans. Figure 3(d) displays the top-gate dependence on electron transport of devices D1 and D2 fabricated on the Au-diffused area, at $T = 2$ K, with top and edge contact, respectively, showing ambipolar transport across what we attribute to be a Dirac point (DP), at gate voltages $V_g = V_D = -1.4$ V (−5.2 V) for D1 (D2). From the gate response, we find that both devices are mildly *n* doped. The gate allows us to tune the carrier density at the level $\alpha = dn_H/dV_g \sim 1.8 \times 10^{11}$ cm^{-2}/V (D1) and 1.7×10^{11} cm^{-2}/V (D2), which agrees well with the dielectric thickness (∼20-nm *h*-BN) and the dielectric constant of the dielectric materials, $\varepsilon_{h\text{-}BN} = 3.76$ and $\varepsilon_{Al_2O_3} = 9$ [24,25]. Figure 3(e) shows Hall carrier density of D1 (D2) at $T = 2$ K at different gate voltages, where the type of the majority carrier shifts from electrons to holes at a gate voltage $V_g = V_D$. The Hall mobility for device D1 is $\mu_H = 200$–250 cm^2/Vs for holes and $\mu_H = 70$–200 cm^2/Vs for electrons; for device D2, somewhat larger mobilities are measured on the electron side, $\mu_H = 500$–600 cm^2/Vs. The gated devices allow us to compare the Hall carrier mobilities with those extracted by the capacitive method using the equation $R_{XX} = \frac{1}{e\mu_C}(\frac{L}{W})\frac{1}{\sqrt{n_g^2+n_0^2}}$, where the e, μ_c, L (W), $n_g = \alpha(V_g - V_D)$, n_0 is electron charge, field-effect mobility, length (width) of the sample, carrier density induced by gate, and residual carrier density, respectively [26]. This capacitor model gives $\mu_c = 270(560)$ cm^2/Vs and $n_0 = 6 \times 10^{11}(7 \times 10^{11})$ electrons/cm^2 for D1 (D2), showing

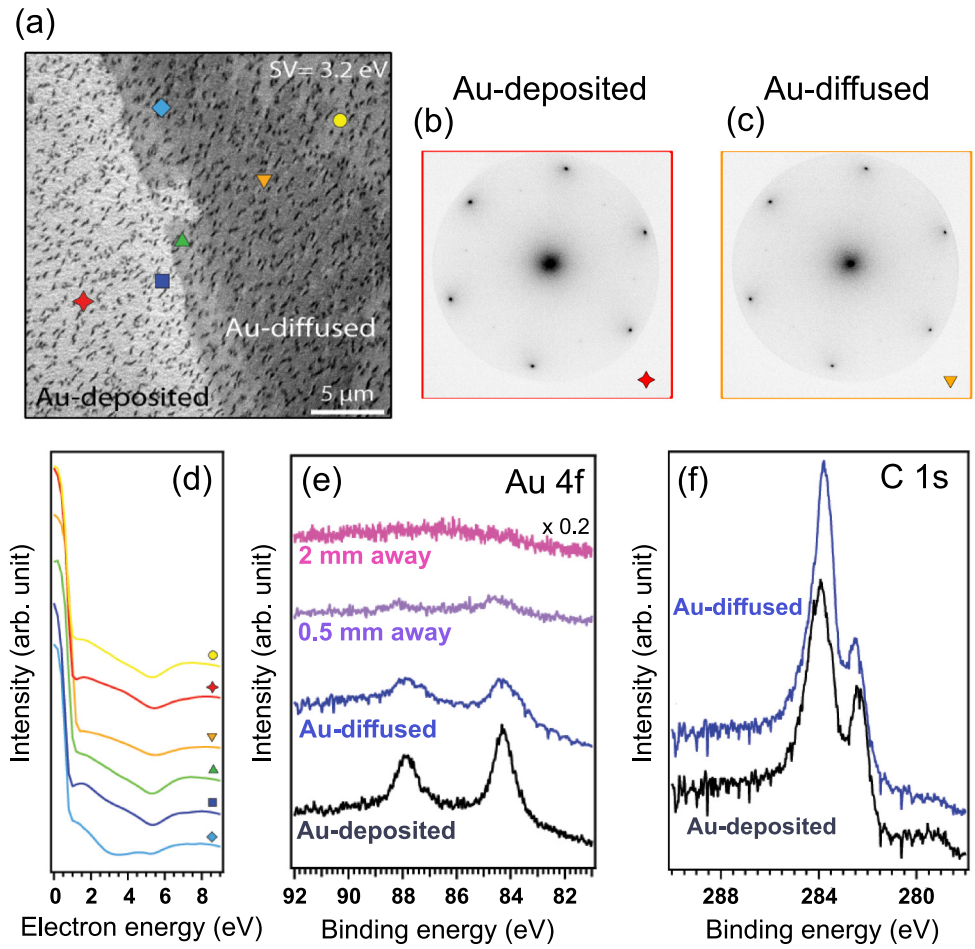

FIG. 2. Synchrotron studies of Au-intercalated quasi-free-standing monolayer graphene. (a) LEEM image (field of view = 25 μm, electron energy 3.2 eV) at the boundary of Au-deposited and Au- diffused areas after Au intercalation ($t_{\mathrm{Au}} = 4$ Å). The black patches in the image were originally monolayer graphene domains (by-product of buffer growth) turned into bilayer after intercalation. (b), (c) Micro-LEED patterns (SV = 45 eV, sampling area 1.5 μm) recorded from the marked areas shown in (a) with corresponding colors and shapes. Au-deposited (b) and diffused (c) regions that show only diffraction from monolayer graphene and no traces of $6\sqrt{3} \times 6\sqrt{3}R30^{\circ}$ structure (which is the fingerprint of the buffer layer). (d) LEEM IV curves from both Au-deposited and Au-diffused areas recorded from the marked areas shown in (a) with corresponding colors and shapes. A dip in the IV LEEM at 5.5 eV is a result of intercalation and consequent formation of free-standing graphene. (e) Micro-XPS spectra ($h\nu = 150$ eV, sampling area 5 μm) of Au $4f$ at different areas show the presence of Au on Au-deposited (black) and diffused (blue) areas and a gradual disappearance of Au signal as the distance from the boundary increases; violet (0.5 mm), pink (2 mm) away, respectively. (f) micro-XPS spectra ($h\nu = 350$ eV, sampling area 5 μm) of C 1s on Au-deposited (black) and diffused (blue) areas.

consistency between μ_{H} and μ_c. Given the residual carrier density n_0 and the $V_{\mathrm{D}} = -1.4$ V (-5.2 V) for D1 (D2), we estimate carrier density at zero-gate voltage $n = \sqrt{n_g^2 + n_0^2} = 7 \times 10^{11}$ (1.2×10^{12}) electrons/cm^2.

With the Hall carrier densities changing from electrons to holes across the DP, we find that asymmetric part of $R_{\mathrm{XY}}(B)$ of D2 at $T = 2$ K shows a weak nonlinearity [Fig. 4(a)] [21]. The nonlinear $R_{\mathrm{XY}}(B)$ allows us to quantify densities and mobilities of electrons and holes using a two-band model. In the presence of both electrons and holes, the conventional Hall resistivity $\rho_{\mathrm{XY}}(B) = -(\frac{1}{e})B\frac{(p\mu_h{}^2 - n\mu_e{}^2) + \mu_h{}^2\mu_e{}^2(p-n)B^2}{(p\mu_h + n\mu_e)^2 + \mu_h{}^2\mu_e{}^2(p-n)^2B^2}$, where n (p) is electron (hole) density and $\mu_{e(h)}$ is the electron (hole) mobility [27,28]. Figures 4(b) and 4(c) show n, p, μ_e, and μ_h extracted by fitting $R_{\mathrm{XY}}(B)$ using the constraint that $\rho_{\mathrm{XX}}(0) = 1/[e(p\mu_h + n\mu_e)]$. The charge-carrier densities (mobilities) of majority carriers extracted from the two-band model are fairly close to the Hall carrier densities n_{H} (Hall mobilities μ_{H}) obtained from the single-carrier model. Figure 4(d) summarizes the ratio n/p and μ_e/μ_h in different gate voltages.

Table I shows a summary of transport properties measured in all the devices. In general, the measured zero-gate doping of Au-intercalated devices is p type, $p = 5 \times 10^{12}$–2×10^{13} holes/cm^2, being higher in magnitude for the Au-deposited regions. The notable exception is for gated devices fabricated on the Au-diffused areas, which show n-type doping. According to Gierz *et al.* [14], Au contents corresponding to 3/8 monolayer (Au-ML) and 1 Au-ML results in highly n-doped ($n = 5 \times 10^{13}$ cm^{-2}) and slightly p-doped [16] ($p = 7 \times 10^{11}$ cm^{-2}) MLG, respectively [15,29]. However, we cannot exclude the possibility of doping of the decoupled MLG during the fabrication processes. Therefore, even for the

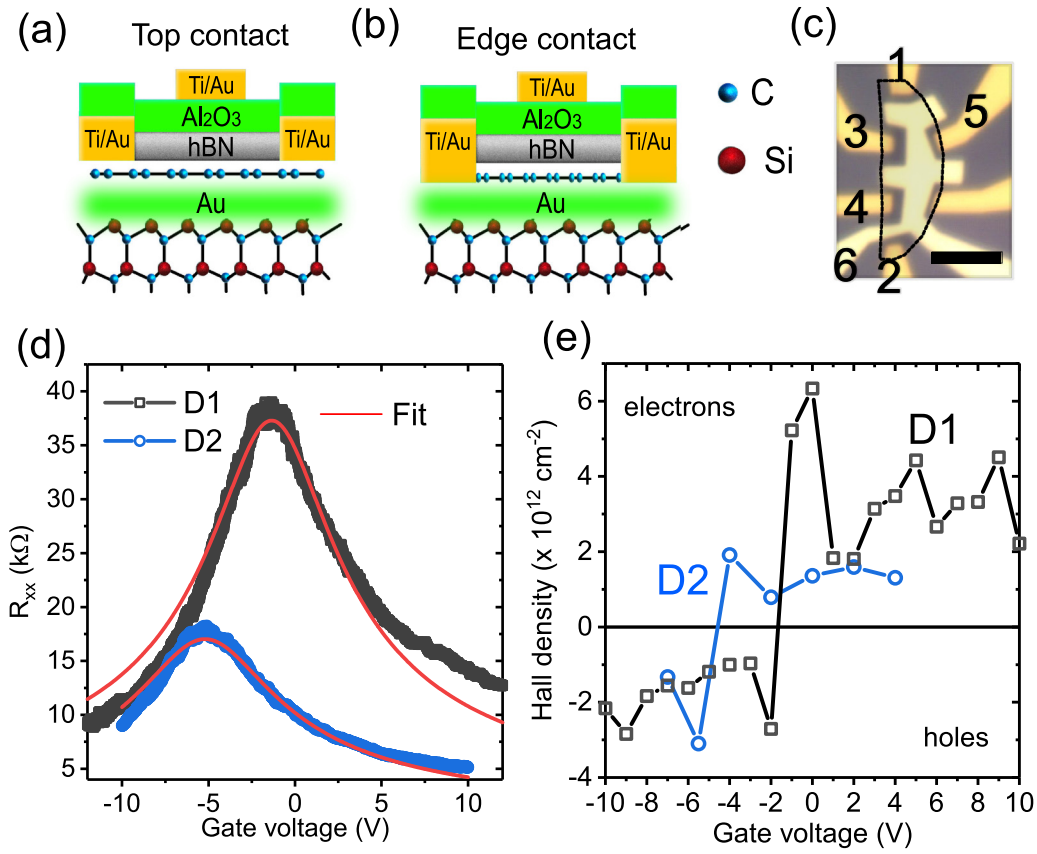

FIG. 3. Electron transport studies on Au-intercalated quasi-free-standing monolayer graphene (a), (b). Schematics of top-gate structures with h-BN/Al_2O_3 gate dielectrics: (a) top contact (D1) and (b) edge contact (D2) configurations. (c) An optical micrograph of D1. The dashed areas indicate the sample covered by h-BN. Measurement configuration: Current bias (1-2), V_{XX} (3-4), V_{XY} (5-3), gate voltage V_g (6-2). The scale bar is 5 μm. (d) Top-gate voltage dependence of the two devices D1 and D2 at $T = 2$ K [$I = 100$ nA (D1) and 1 μA (D2)] showing Dirac points in both devices. The red lines are the fitted curves to the equation, $R_{XX} = \frac{1}{e\mu_C}(\frac{L}{W})\frac{1}{\sqrt{n_g^2+n_0^2}}$. (e) Gate-voltage dependence of Hall carrier density of D1 (black, $I = 100$ nA) and D2 (blue, $I = 1$ μA) at $T = 2$ K, showing transition from electrons to holes across the DP.

thicker Au layer ($t_{Au} = 8$ Å), we cannot attribute the measured p doping solely to the Au content [15]. While gated devices allow us to explore the carrier mobility as a function of the gate voltage, the mobilities of other devices at a fixed carrier density do not exceed 100 cm^2/Vs. We note that the reported mobility of hydrogen-intercalated Bu-L is on the order of 1000 cm^2/Vs [9–12], suggesting the possibility that the relatively low mobility is intrinsic in Bu-L as a consequence of defects on the as-grown Bu-L [30] or of an imperfect intercalation process.

C. Spin-orbit scattering effects

Despite the presence of Au atoms in proximity to the QFS graphene layer, spin-orbit scattering effects are not readily manifested in our devices by magnetotransport measurements. Figure 5 shows a representative example of the magnetoconductivity measured in all our devices at $T = 2$ K. To mention, the observation of *positive* magnetoconductance (i.e., weak localization) suggest either the lack of spin-orbit effects in the Au-intercalated QFS graphene system, or that Au atoms induce $z \rightarrow -z$ symmetric SO coupling in graphene [31].

TABLE I. Summary of measured devices.

Dev.	t_{Au}(Å)	Region	Doping type	Carrier density (10^{12} cm^{-2})	Mobility (cm^2/Vs)	V_D(V)
D1	4	Au diffused	Electron	0.7	210	−1.4
D2	4	Au diffused	Electron	1.2	560	−5.2
D3	4	Au deposited	Hole	10	90	
D4	4	Au deposited	Hole	10	80	
D5	8	Au diffused	Hole	7	30	
D6	8	Au diffused	Hole	5	90	
D7	8	Au deposited	Hole	10	50	
D8	8	Au deposited	Hole	20	15	

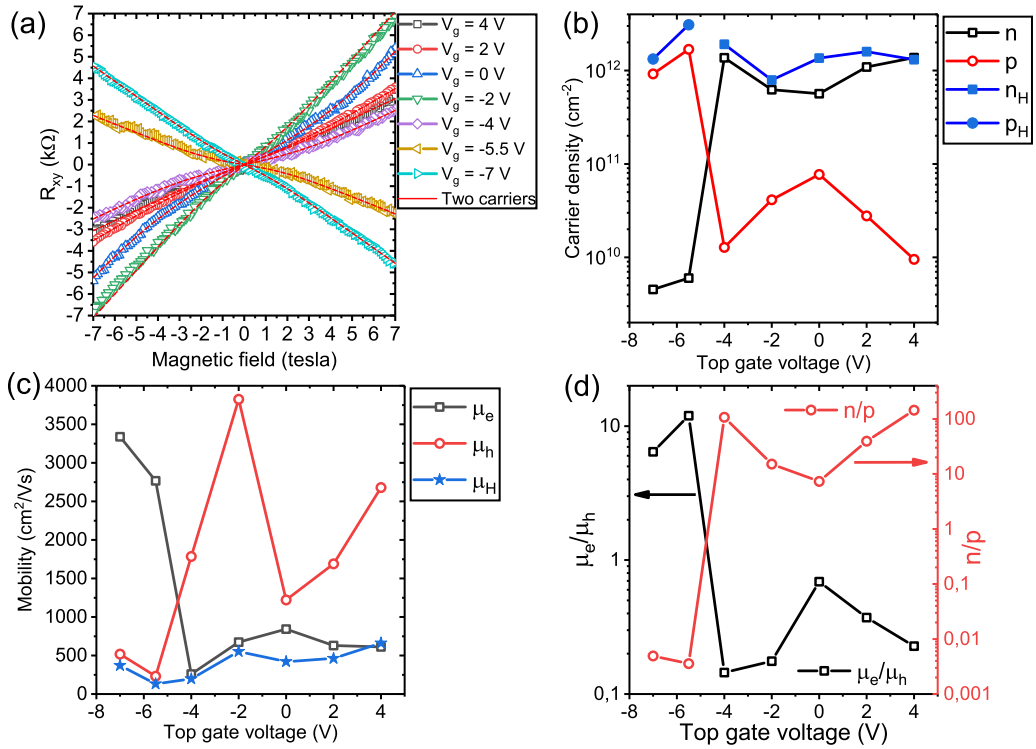

FIG. 4. Two-charge-carrier analysis. (a) Asymmetric parts of $R_{XY}(B)$ of D2 at $T = 2$ K at different top-gate voltages. Red lines are fits to our experimental data using a two-band model, with $\rho_{XY}(B) = -(\frac{1}{e})B\frac{(p\mu_h{}^2 - n\mu_e{}^2)+\mu_h{}^2\mu_e{}^2(p-n)B^2}{(p\mu_h+n\mu_e)^2+\mu_h{}^2\mu_e{}^2(p-n)^2B^2}$, in which n (p) and μ_e (μ_h) are the electron (hole) densities and mobilities, respectively. (b) Gate-voltage dependence of n, p, and Hall electron (hole) density $n_H(p_H)$ obtained from the single-carrier model. (c) Gate-voltage dependence of μ_e, μ_h, and Hall mobilities μ_H obtained from the single-carrier model. (d) μ_e/μ_h and n/p at different gate voltages.

With a gate-dependent momentum relaxation length $L_p = h/(2e^2\rho_{XX}\sqrt{n\pi})$ in the range 2–5 nm (3–8 nm) for D1 (D2), the curvature κ of the low-field magnetoconductance [32,33] $\kappa = \frac{\partial^2\sigma_{XX}}{\partial B^2}|_{B=0} = \frac{16\pi}{3}\frac{e^2}{h}(\frac{D\tau_\varphi}{h/e})^2$, where h is the Planck constant and D is the diffusion coefficient, allows us to quantify a phase-relaxation time in the range $\tau_\varphi = 0.7$–3.4 ps (dephasing length $L_\varphi = 33$–42 nm) for D1 and $\tau_\varphi = 0.4$–0.7 ps ($L_\varphi = 30$–39 nm) for D2 (see Fig. S9 for gate dependence) [21]. With the short phase-relaxation time and the overall low mobility in the samples, we argue that for our devices, disorder (i.e., lack of range order in intercalated Au atoms) could obscure the observation of SOI in magnetotransport. In fact, it is only for devices fabricated on the substrate containing $t_{Au} = 4$ Å that the temperature dependence of conductivity is close to logarithmic (Fig. S10) [21], implying that quantum interference corrections are visible only on those devices. However, if the phase-relaxation time is shorter than the spin-orbit scattering time $\tau_{SO} > \tau_\varphi$, the effects of spin-orbit scattering might not be observable in our samples under the measurement conditions (down to $T = 2$ K). In general, the SOI enhancement of MLG in proximity to Au is affected by the structure of graphene-Au interfaces including hybridization of orbitals, graphene-Au distances, and position of Au with respect to the graphene lattice [16,34–37]. Band calculations predict that the optimal configuration for SOI enhancement is that of Au atoms located at hollow sites of graphene [16,34]. Therefore, it is likely that the observation of positive magnetoconductance in our samples might be related to the Au atoms occupying random sites at the Bu-L/SiC interface. Moreover, it appears that the excess of gold contributes to enhancing the disorder in the samples. The temperature dependence of

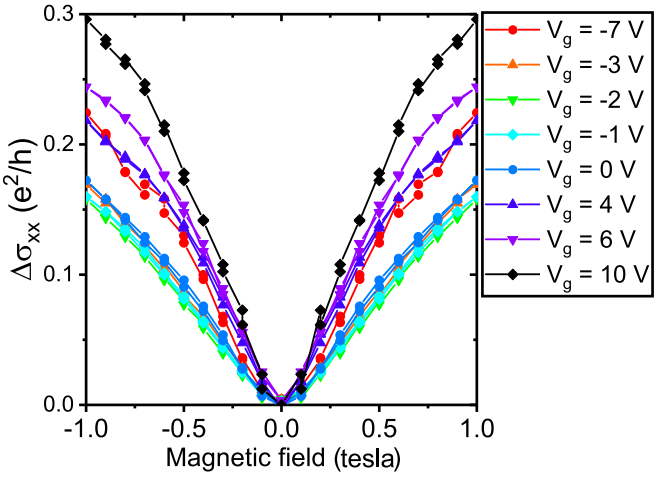

FIG. 5. Positive magnetoconductivity. Symmetrized longitudinal magnetoconductivity $\Delta\sigma_{XX} = \sigma_{XX}(B)$–$\sigma_{XX}(0)$ of D1 at $T = 2$ K (current bias $I = 100$ nA) at different gate voltages shows positive magnetoconductance. (See Fig. S7 for details of symmetrization [21].)

devices fabricated with QFS graphene with higher Au content ($t_{Au} = 8$ Å) follows the characteristic dependence of granular metals [38] and variable range hopping [39]: $R(T) = R_0 \exp[(T_0/T)^{1/2}]$, with $T_0 = 30$–100 K and $R_0 = 3$–9 kΩ for device D5, D6, and D7, and $R(T) = R_0 \exp[(T_0/T)^{1/4}]$, with $T_0 = 320$ K and $R_0 = 7$ kΩ for device D8, suggesting that excess gold introduces additional sources of momentum and energy relaxation of carriers.

III. CONCLUSIONS

In conclusion, we show that Au-intercalated QFS monolayer graphene can be obtained by deposition of one or few gold monolayers on the Bu-L surface followed by annealing in Ar atmosphere. Au can diffuse under the Bu-L surface and this leads to diluted contents of Au millimeters away from the Au-deposited area. Au-intercalated QFS monolayer graphene samples are stable in ambient conditions and allow for the *ex situ* fabrication of devices and material characterization. Intercalation of Au atoms at the buffer/SiC is a highly reproducible process and therefore of highly technological relevance. By decoupling it from the substrate, the Au-intercalated monolayer graphene shows pronounced gate modulation of conductance, with a Dirac point at $V_D = -1.4$ and -5.2 V (carrier density at $V_g = 0$ is $n = 7 \times 10^{11}$ and 1.2×10^{12} electrons/cm^2). Future efforts in samples where an optimized thermal drive-in step leads to ordered Au atoms at the graphene-SiC interface [15,16] are needed to reveal if SOI signatures will manifest in the electron transport properties of graphene, similar to reports for Au-intercalated graphene on nickel substrate [16] and van der Waals heterostructures of graphene and transition-metal dichalcogenides [40].

IV. EXPERIMENTAL METHODS

A. Growth of Bu-L on SiC

The carbon buffer is an integral part of the epitaxial graphene-SiC material system and is the first to form when SiC substrate is exposed to high temperature ($T > 1500$ °C). More specifically, this is the carbon-rich surface reconstruction ($6\sqrt{3} \times 6\sqrt{3}$) characteristic of Si face SiC at elevated temperatures. To prevent the growth of graphene and grow only the carbon buffer layer, here we used 7×7 mm^2 4*H*-SiC substrates and applied gradual (inductive) heating in argon atmosphere until $T \approx 1700$ °C was reached and that kept for 30 s. Then the furnace was switched off and the samples were taken out at room temperature. Prior to growth, the chamber was pumped down to a base pressure of $P_0 = 1 \times 10^{-6}$ mbar in order to minimize oxygen contamination which is detrimental for a complete carbonization.

B. Au deposition

Metals were deposited by e-beam evaporation at base pressure $P_0 = 5 \times 10^{-7}$ mbar in a Lesker PVD 225 fitted with a custom-built substrate heater. Deposition on part of the substrate took place through a shadow mask, to avoid surface contamination. Before metal deposition, the substrate temperature is raised to 200 °C and kept constant for 5 min. The deposition rate is set to $r = 1$ Å/s, yielding a deposition time of 4 and 8 s, for $t_{Au} = 4$ Å and $t = 8$ Å, respectively.

C. Intercalation

Substrates were heated up in an atmosphere of ultrapure argon of $P_0 = 800$ mbar at $T = 850$ °C for 90 min. Lower temperatures resulted in partial intercalation of Au, while at higher temperatures the intercalated Au layer can escape the interface.

D. LEEM and micro-XPS

Low-energy electron microscopy experiments were performed at MAXPEEM beamline at MAX IV synchrotron facility (1.5-GeV ring), Lund, Sweden. The beamline is housing aberration-corrected spectroscopic photoemission and low-energy electron microscope. The microscope has a plethora of imaging modes, which is capable of delivering information on structural, chemical, electronic, and magnetic contrast at spatial resolutions in the nanometer range in one instrument. In addition to imaging modes, microspectroscopy measurements are possible, allowing acquisition of micro-XPS spectra from an area of interest in the 1–10-μm range.

E. STM

STM measurements were carried out at NPL on an ultrahigh-vacuum LT Nanoprobe Scienta Omicron system, base pressure 4×10^{-11} mbar, at room temperature, with no prior surface conditioning of the sample. The images were recorded at a tunneling current of 1 nA and a bias voltage of -0.4 V, using electrochemically etched W wires.

F. Microfabrication

To fabricate top-gate devices, *h*-BN flakes dehydrated by baking at 200 °C for 20 min in nitrogen atmosphere were mechanically exfoliated on top of the Au-intercalated Bu-L prebaked at 200 °C for 10 min in nitrogen. The exfoliated substrate was directly transferred to the furnace and annealed at 750 °C for 1 h in vacuum to remove hydrocarbon impurities and water at the interface. D2 was edge contacted by oxygen plasma etching followed by contacting with Ti/Au (5/80 nm) after EBL, and other devices were top contacted by contacting with Ti/Au (5/80 nm) after EBL followed by oxygen plasma etching.

ACKNOWLEDGMENTS

This work was jointly supported by the Swedish Foundation for Strategic Research (SSF) (Grants No. IS14-0053, No. GMT14-0077, and No. RMA15-0024), the Korean-Swedish Basic Research Cooperative Program of the NRF, Korea (Grant No. NRF-2017R1A2A1A18070721), Knut and Alice Wallenberg Foundation, and Chalmers Area of Advance NANO. This work was performed in part at Myfab Chalmers. This project has received funding from the European Union's Horizon 2020 research and innovation programme Graphene Flagship under Grant Agreement No. 881603.

[1] C. Virojanadara, M. Syväjarvi, R. Yakimova, L. I. Johansson, A. A. Zakharov, and T. Balasubramanian, Phys. Rev. B **78**, 245403 (2008).

[2] K. V. Emtsev, A. Bostwick, K. Horn, J. Jobst, G. L. Kellogg, L. Ley, J. L. McChesney, T. Ohta, S. A. Reshanov, J. Röhrl, E. Rotenberg, A. K. Schmid, D. Waldmann, H. B. Weber, and T. Seyller, Nat. Mater. **8**, 203 (2009).

[3] S. Kopylov, A. Tzalenchuk, S. Kubatkin, and V. I. Fal'ko, Appl. Phys. Lett. **97**, 112109 (2010).

[4] K. Takase, S. Tanabe, S. Sasaki, H. Hibino, and K. Muraki, Phys. Rev. B **86**, 165435 (2012).

[5] H. He, K. H. Kim, A. Danilov, D. L. Y. Montemurro, Y. W. Park, F. Lombardi, T. Bauch, K. Moth-Poulsen, T. Iakimov, R. Yakimova, P. Malmberg, C. Müller, S. Kubatkin, and S. Lara-Avila, Nat. Commun. **9**, 3956 (2018).

[6] J. Ristein, S. Mammadov, and T. Seyller, Phys. Rev. Lett. **108**, 246104 (2012).

[7] C. Riedl, C. Coletti, T. Iwasaki, A. A. Zakharov, and U. Starke, Phys. Rev. Lett. **103**, 246804 (2009).

[8] C. Riedl, C. Coletti, and U. Starke, J. Phys. D Appl. **43**, 374009 (2010).

[9] S. Tanabe, M. Takamura, Y. Harada, H. Kageshima, and H. Hibino, Appl. Phys. Express **5**, 125101 (2012).

[10] F. Speck, J. Jobst, F. Fromm, M. Ostler, D. Waldmann, M. Hundhausen, H. B. Weber, and T. Seyller, Appl. Phys. Lett. **99**, 122106 (2011).

[11] D. Waldmann, J. Jobst, F. Speck, T. Seyller, M. Krieger, and H. B. Weber, Nat. Mater. **10**, 357 (2011).

[12] F. Speck, M. Ostler, J. Röhrl, J. Jobst, D. Waldmann, M. Hundhausen, L. Ley, H. B. Weber, and T. Seyller, Mater. Sci. Forum **645–648**, 629 (2010).

[13] N. Briggs, Z. M. Gebeyehu, A. Vera, T. Zhao, K. Wang, A. De La Fuente Duran, B. Bersch, T. Bowen, K. L. Knappenberger, and J. A. Robinson, Nanoscale **11**, 15440 (2019).

[14] I. Gierz, T. Suzuki, R. T. Weitz, D. S. Lee, B. Krauss, C. Riedl, U. Starke, H. Höchst, J. H. Smet, C. R. Ast, and K. Kern, Phys. Rev. B **81**, 235408 (2010).

[15] S. Forti, S. Link, A. Stöhr, Y. Niu, A. A. Zakharov, C. Coletti, and U. Starke, Nat. Commun. **11**, 2236 (2020).

[16] D. Marchenko, A. Varykhalov, M. R. Scholz, G. Bihlmayer, E. I. Rashba, A. Rybkin, A. M. Shikin, and O. Rader, Nat. Commun. **3**, 1232 (2012).

[17] A. Varykhalov, J. Sánchez-Barriga, A. M. Shikin, C. Biswas, E. Vescovo, A. Rybkin, D. Marchenko, and O. Rader, Phys. Rev. Lett. **101**, 157601 (2008).

[18] A. Varykhalov, J. Sánchez-Barriga, D. Marchenko, P. Hlawenka, P. S. Mandal, and O. Rader, Nat. Commun. **6**, 7610 (2015).

[19] J. Park, H. D. Yun, M. J. Jin, J. Jo, I. Oh, V. Modepalli, S. Y. Kwon, and J. W. Yoo, Phys. Rev. B **95**, 245414 (2017).

[20] K. H. Kim, H. He, M. Rodner, R. Yakimova, K. Larsson, M. Piantek, D. Serrate, A. Zakharov, S. Kubatkin, J. Eriksson, and S. Lara-Avila, Adv. Mater. Interfaces **7**, 1902104 (2020).

[21] See Supplemental Material at http://link.aps.org/supplemental/10.1103/PhysRevB.102.165403 for additional AFM, LEEM, and LEED data, electrical probing of intercalation processes, optical photographs of microdevices D1 to D8, magnetotransport data of D2, gate dependence of weak localization fit parameters, and temperature dependence of conductivity and resistance of Au-intercalated QFS graphene.

[22] T. Yager, A. Lartsev, S. Mahashabde, S. Charpentier, D. Davidovikj, A. Danilov, R. Yakimova, V. Panchal, O. Kazakova, A. Tzalenchuk, S. Lara-Avila, and S. Kubatkin, Nano Lett. **13**, 4217 (2013).

[23] H. Hibino, H. Kageshima, F. Maeda, M. Nagase, Y. Kobayashi, and H. Yamaguchi, Phys. Rev. B **77**, 075413 (2008).

[24] A. Laturia, M. L. Van de Put, and W. G. Vandenberghe, Npj 2D Mater. Appl. **2**, 6 (2018).

[25] J. Robertson, Eur. Phys. J. Appl. Phys. **28**, 265 (2004).

[26] S. Kim, J. Nah, I. Jo, D. Shahrjerdi, L. Colombo, Z. Yao, E. Tutuc, and S. K. Banerjee, Appl. Phys. Lett. **94**, 062107 (2009).

[27] J. S. Kim, S. S. A. Seo, M. F. Chisholm, R. K. Kremer, H.-U. Habermeier, B. Keimer, and H. N. Lee, Phys. Rev. B **82**, 201407(R) (2010).

[28] A. Nachawaty, M. Yang, W. Desrat, S. Nanot, B. Jabakhanji, D. Kazazis, R. Yakimova, A. Cresti, W. Escoffier, and B. Jouault, Phys. Rev. B **96**, 075442 (2017).

[29] G. Giovannetti, P. A. Khomyakov, G. Brocks, V. M. Karpan, J. van den Brink, and P. J. Kelly, Phys. Rev. Lett. **101**, 026803 (2008).

[30] T. A. de Jong, E. E. Krasovskii, C. Ott, R. M. Tromp, S. J. van der Molen, and J. Jobst, Phys. Rev. Mater. **2**, 104005 (2018).

[31] E. McCann and V. I. Fal'ko, Phys. Rev. Lett. **108**, 166606 (2012).

[32] S. Lara-Avila, S. Kubatkin, O. Kashuba, J. A. Folk, S. Lüscher, R. Yakimova, T. J. B. M. Janssen, A. Tzalenchuk, and V. Fal'ko, Phys. Rev. Lett. **115**, 106602 (2015).

[33] E. McCann, K. Kechedzhi, V. I. Fal'ko, H. Suzuura, T. Ando, and B. L. Altshuler, Phys. Rev. Lett. **97**, 146805 (2006).

[34] A. López, L. Colmenárez, M. Peralta, F. Mireles, and E. Medina, Phys. Rev. B **99**, 085411 (2019).

[35] F. C. Chuang, W. H. Lin, Z. Q. Huang, C. H. Hsu, C. C. Kuo, V. Ozolins, and V. Yeh, Nanotechnology **22**, 275704 (2011).

[36] A. Bayani and K. Larsson, Sci. Rep. **10**, 1042 (2020).

[37] C. H. Hsu, W. H. Lin, V. Ozolins, and F. C. Chuang, Appl. Phys. Lett. **100**, 063115 (2012).

[38] B. Abeles, P. Sheng, M. D. Coutts, and Y. Arie, Adv. Phys. **24**, 407 (1975).

[39] K. H. Kim, S. Lara-Avila, H. He, H. Kang, S. J. Hong, M. Park, J. Eklöf, K. Moth-Poulsen, S. Matsushita, S. Kazuo Akagi, S. Kubatkin, and Y. W. Park, Sci. Rep. **8**, 4948 (2018).

[40] Z. Wang, D.-K. Ki, J. Y. Khoo, D. Mauro, H. Berger, L. S. Levitov, and A. F. Morpurgo, Phys. Rev. X **6**, 041020 (2016).